Solvation-Induced Onsager Reaction Field Rather than Double Layer Field Controls CO_2 Reduction on Gold

Quansong Zhu[1,+], Spencer Wallentine[1,+], Gang-Hua Deng[1], and L. Robert Baker[1,*]

[1]Department of Chemistry and Biochemistry, The Ohio State University, Columbus, Ohio, USA
[*]baker.2364@osu.edu
[+]these authors contributed equally to this work

ABSTRACT

The selectivity and activity of the carbon dioxide reduction reaction (CO_2R) are sensitive functions of the electrolyte cation. By measuring the vibrational Stark shift of in-situ generated CO on Au in the presence of alkali cations, we quantify the total electric field present during turnover and deconvolute this field into contributions from 1) the electrochemical Stern layer and 2) the Onsager, or solvation-induced, reaction field. The magnitude of the Onsager field is shown to be on the same order as the Stern layer field ($\sim$10 MV/cm) but follows an opposite trend with cation, increasing from $Li^+ < Na^+ < K^+ < Rb^+ \approx Cs^+$. Contrary to theoretical reports, CO_2R kinetics are not correlated with the Stern field but instead are controlled by the strength of the Onsager reaction field with Cs^+ as an exception. Spectra of interfacial water as a function of cation show that Cs^+ induces a change in the interfacial water structure correlated with a dramatic drop in CO_2R activity, highlighting the importance of cation-dependent interfacial water structure on reaction kinetics. These findings show that both the Onsager reaction field and interfacial solvation structure must be explicitly considered for accurately modeling of CO_2R reaction kinetics.

Introduction

Electrocatalytic CO_2 reduction (CO_2R) has received widespread attention because it is a promising method to convert excess CO_2 in the atmosphere to industrial feedstocks. Despite numerous reports on the topic, mechanistic understanding of this process, is limited. Additionally, CO_2R kinetics are slow and must compete with H_2 evolution in aqueous electrolytes, which limits its practical application. Alkali cations are known to increase the selectivity and activity of CO_2R significantly, however, the fundamental reason for this observation is still under debate. Understanding the cation dependence would provide much needed insights to help make CO_2R economically viable.

Several explanations have been put forward regarding the effect of cations on CO_2R. To avoid confusion, we note that the terms used in this paper describing the relative size of cations, e.g. larger and smaller, are based on the crystal radii of the cations, which increases from Li^+ to Cs^+. Bell et al. propose that water molecules coordinated to larger cations possess a lower pKa.[1] They argue that this makes the interfacial pH more acidic thereby increasing the local CO_2 concentration due to bicarbonate equilibrium. The effect of local buffering has been verified experimentally,[2] however Xu et al. measured the local CO_2 concentration and found that it was highest for smaller cations, in contradiction to the prediction by Bell et al.[3] Another consideration has been put forward by Norskov et al.[4,5] which indicates that cations create a local electric field that can stabilize bending of CO_2 through field-dipole interactions. This interaction fosters the adsorption of CO_2 as the field in the electrochemical double layer increases.[5] In support of this hypothesis, Chan and co-workers recently showed that multi-scale-modeling of interactions between a CO_2 dipole and the potential-dependent electric field can reproduce the observed Tafel slope for CO_2R on Au.[6]

However, at electrochemical interfaces there are multiple fields present. This includes the electric field produced by formation of the electrochemical double layer described within the Gouy-Chapman-Stern (GCS) formalism, where the electrolyte is ordered with an inner Stern layer and an outer diffuse layer.[7] The ions in the electrolyte can approach the electrode but have a finite size and the distance of closest approach is known as the outer helmholtz plane (OHP). The OHP divides the Stern layer from the diffuse layer. Measuring Stark shifts for small adsorbed molecules such as CO represents a measure of the electric field present with the Stern layer, and we have recently shown that measured Stark shifts for CO on Au qualitatively match predictions from GCS theory.[8] However, in addition to the Stern layer field, the absolute Stark shift will also include contributions due to the Onsager reaction field, which is induced by polarization of the electrolyte by the solute dipole.[9] This Onsager reaction field can have a similar magnitude as the field created by the double layer and should not be neglected when considering the effect of electric field on CO_2R reaction kinetics.

To yield further insight into this important question, we have directly probed the interfacial electric field during CO_2R electrocatalysis using in-situ generated CO on Au as a vibrational Stark reporter. To overcome the challenge of low surface coverage for in-situ generated CO, the electric field at Au active sites is monitored here using plasmon-enhanced vibrational sum frequency generation spectroscopy (VSFG) as described recently.[8, 10] Both the Stern and Onsager fields are measured as a function of applied potential in 0.1 M cation bicarbonate electrolyte with the following alkali cations: Li^+, Na^+, K^+, Rb^+, and Cs^+.

In contradiction to predictions that larger cations induce a stronger local field in the electrochemical double layer, these measurements show that the Stern layer field reaches the highest magnitude in the presence of Li^+ and decreases in the order $Li^+ > Na^+ > K^+ > Rb^+$. In contrast, the Onsager reaction field increases from Li^+ to Rb^+. Notably, Cs^+ breaks the trend for both Stern layer electric field and Onsager reaction field, and analysis indicates that Cs^+ specifically adsorbs on the Au surface. Interestingly, the CO_2R activity follows the same trend as the Onsager reaction field rather than the Stern field, suggesting that interfacial solvation structure and its associated electric field play a critical role in CO_2 activation. To confirm this conclusion, we additionally measure the cation-dependent interfacial water spectra using VSFG spectroscopy. To our knowledge, these represent the first VSFG spectra of interfacial water reported during electrocatalysis. These show that Cs^+ induces a change in the interfacial water structure correlated with a dramatic drop in CO_2R activity despite Cs^+ displaying the strongest total (Stern + Onsager) electric field, highlighting the importance of cation-dependent interfacial water structure on reaction kinetics.

Results

At potentials away from the potential of zero charge (PZC) an electric field is created due to the applied charge on the electrode and the oppositely charged ions in solution as shown in Figure 1a. This electric field decays as a function of distance from the electrode, and is called the double layer (DL) electric field. This field can further be broken down into contributions from an inner Stern layer electric field, and an outer diffuse layer electric field. In this paper we directly measure the Stern Layer electric field as our probe is located in the Stern layer.[8] At potentials relevant to CO_2R, the Stern field typically has a magnitude on the order of tens of MV/cm.

Also present for polar solutes in polarizable media is the Onsager reaction field.[11] This field occurs through interaction of the solute dipole with the surrounding solvent and ions, where the solute dipole induces image dipoles in the surrounding medium (Figure 1b). These solvent dipoles, in turn, sum to a net image dipole, or "reaction field", which can be of similar magnitude as the Stern layer field.[9] Notable work has been made by Dawlaty et al. to extend this model to interfaces, which are inherently asymmetric.[9] When it comes to CO_2 reduction, CO and other polar intermediates will experience an Onsager reaction field from the surrounding solvent and alkali cations. Both the Stern layer field and the Onsager reaction field are present at electrochemical interfaces, as shown in Figure 1c, and we will show that it is possible and important to disentangle these fields in order to separately consider their contributions to CO_2R.

Here we measure the interfacial electric field using in-situ generated CO, which resides in the Stern layer, and changes vibrational frequency in an electric field due to the vibrational Stark effect. The associated spectra are in the supporting information section 1. By measuring the vibrational frequency ($\omega(\phi)$) as a function of potential (ϕ), and with an appropriate reference frequency (ω_{ref}), we can determine the interfacial electric field ($\vec{F}(\phi)$) as shown in Equation 1.

$$\omega(\phi) = \omega_{ref} - \vec{\Delta\mu} \cdot \vec{F}(\phi) \tag{1}$$

The Stark tuning rate ($\Delta\mu$) of CO is a constant and has been measured previously.[8, 12] The choice of reference frequency is important, and allows us to separate the Stern layer electric field from the Onsager reaction field.[13] In Figure 1d - f we use the CO frequency data of K^+ as an example to show how we disentangle these two contributions to the total field. Since the net electrode charge is minimized at the PZC, the Stern layer electric field will also be at a minimum. Thus, by choosing the frequency at the PZC as our reference point (ω_{ref} in Equation 1) we can obtain the contribution of the Stern layer electric field to the total field at each potential (Figure 1d). As it is not possible to measure the in-situ generated CO frequency at the PZC due to the negligible activity of CO_2R at this positive potential, the extrapolated frequency at the PZC is used. The PZC was determined by measuring the capacitance minimum with impedance spectroscopy and occurs for all alkali cations near -0.1 V vs. Ag/AgCl. The details of PZC determination are discussed in the method section 3, and the corresponding capacitance data is provided in the supporting information section 2. Alternatively, by referencing the extrapolated frequency at PZC to the frequency of CO adsorbed to Au in vacuum (2126 cm^{-1}), an estimate of the Onsager reaction field felt by the solvated CO reporter can be obtained (Figure 1e).[9, 14] Here we note that the magnitude of the Onsager reaction field may change with potential due to a decreasing dielectric constant. However, at fields greater than 10 MV/cm, this change becomes minimal.[15] As shown in Figure 2b, most of the cations have reached the 10 MV/cm threshold near -0.3 V, so it is reasonable to assume that the observed Stark shift at more negative potentials comes mainly from the Stern layer electric field, and not from potential-induced
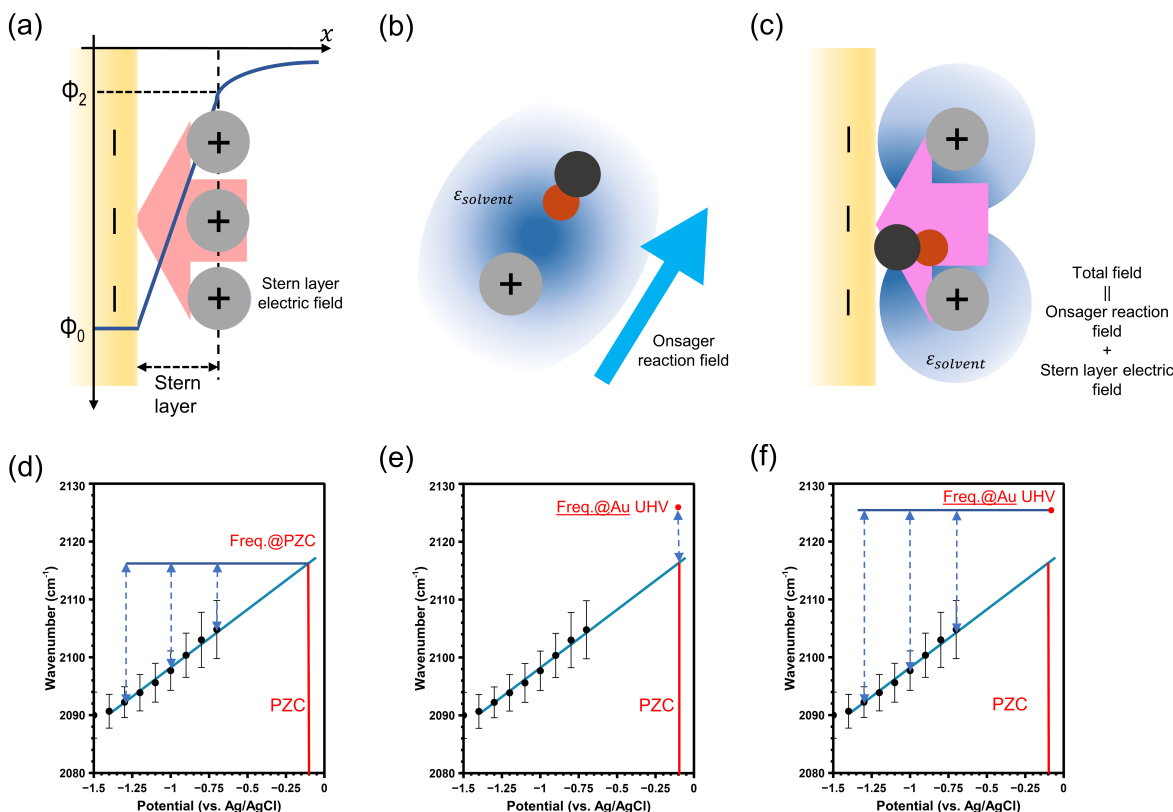
Figure 1. a) Diagram of Stern layer electric field at the electrode surface; b) Diagram of Onsager reaction field in the bulk solution. The black circle represents the carbon atom, while the red circle represents the oxygen atom; c) Diagram of Total field at the electrode surface with contributions from both Onsager reaction field and Stern layer electric field; d) Calculation of Stern layer electric field by referencing CO frequency under each potential to extrapolated frequency at PZC; e) Calculation of Onsager reaction field by referencing extrapolated frequency at PZC to frequency of CO adsorbed on Au in vacuum; f) Calculation of total field by referencing CO frequency under each potential to frequency of CO adsorbed on Au in vacuum.

perturbations to the Onsager reaction field. The total field present at the electrochemical interface is the sum of the Onsager and Stern fields. The total field magnitude can be obtained by referencing the CO frequency under each potential to the frequency of CO adsorbed to Au in vacuum (Figure 1f).

According to this method for separating individual contributions to the sum total electric field, all effects of CO solvation, including H-bonding, will be combined in the Onsager reaction term. This is the result of referencing the frequency shift at the PZC to the CO frequency in vacuum such that the Onsager term quantified here includes both the pure polarization field plus effects of explicit solvation in aqueous electrolyte. H-bonding in π systems induce frequency shifts due to changes in occupancy of molecular orbitals.[9,16,17] Although not purely a Stark effect, this is commonly quantified in terms of the equivalent field required to induce the observed frequency shift. Previous work indicates that H-bonding interactions will have a relatively minor effect on the CO vibrational frequency,[12,18,19] compared to CN-bases Stark reporters where H-bonding shifts are significant.[9] This indicates that the Onsager reaction fields reported here are expected to be primarily the result of electrolyte polarization, although contributions from explicit solvent interactions should not be ignored. Although it is not possible in present measurements to fully disentangle these effects, it is still useful to consider the electric field equivalence induced by the combination of electrolyte polarization plus solvent interactions in order to compare the effects of Onsager reaction field and the Stern layer electric field on CO_2R kinetics as discussed below.

We apply the deconvolution method above to all alkali cations, and the calculated total electric field, Stern layer field, and Onsager reaction field, are shown in Figure 2a, b, and c, respectively. As shown in Figure 2a, these alkali cations exhibit total fields of similar magnitude, but Cs^+ has the highest total field. This result is similar to the results of Weagele et al.[20], which shows the total field slightly increases from Li^+ to Cs^+. However, by deconvolution of the Stern layer electric field and Onsager field we find insightful trends. As shown in Figure 2b, at catalytic potentials the Stern layer electric field strength is

largest for Li^+, and decreases going from Li^+ to Rb^+, and then increases again for Cs^+. Ignoring Cs^+, this trend is inversely correlated with the crystal radii of alkali cations. According to GCS theory the slope of these Stark tuning curves is inversely proportional to the distance between the electrode surface and the OHP, which can be equated to the radius of the adsorbed (hydrated) cations. This trend shows that adsorbed Li^+ displays the smallest radius and that cation size increases going from Li^+ to Rb^+. Although this follows the expectation for crystal radii of the respective cations, it is opposite the trend expected based on solvated radii as determined by bulk diffusivity measurements,[21,22] indicating that these ions retain only a portion of their hydration sphere upon adsorption. This ordering also contradicts recent theoretical calculations indicating that CO_2R kinetics are controlled primarily by the strength of the Stern layer electric field.[5,6,23]

Figure 2c shows the Onsager contribution to the total electric field as a function of cation. Interestingly, this Onsager reaction field follows nearly the opposite trend from the Stern field, increasing with cation size from Li^+ to $Rb^+ \approx Cs^+$. This result is consistent with the expected contribution of cation polarizability to the Onsager field, where larger, more polarizable cations will result in a larger reaction field in the presence of a similar dipole. We note that Cs^+ is an anomaly in terms of the Stern layer field. Cs^+ also deviates slightly from the observed trend in Onsager field although to a lesser extent. We attribute this behavior of Cs^+ to its specific adsorption, which decreases the distance between electrode surface and OHP, and this will be discussed in greater detail below.
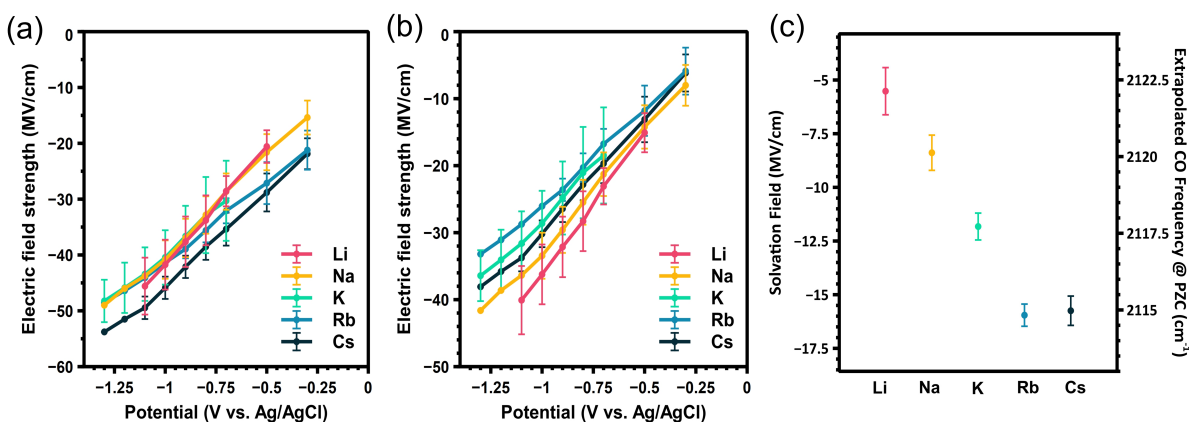

Figure 2. a) Total field strength with applied potential; b) Stern layer electric field strength with applied potential; c) Extrapolated CO frequency at PZC and corresponding reaction field strength calculated as referenced to the frequency of CO adsorbed to Au in vacuum.[14] Error bars in panels a and b represent a standard deviations from multiple experiments. Error bars in panel c are derived from error in the slope.

Disentangling these separate contributions to the total measured electric field provides important insights into the cation-dependent structure of the DL. For example, the Stern layer thickness, or distance from the electrode surface to the OHP, is inversely proportional to the magnitude of the Stern layer electric field at an applied potential. Because CO adsorbed on Au resides in the Stern layer, the Stark tuning slope is a sensitive function of the Stern layer thickness. Using the slope for each cation, we determine the potential at the OHP and the size of the Stern Layer using Gouy-Chapman-Stern (GCS) theory as described in the methods section 4.[24] Table S1 in the supporting information section 3 provides the results of the GCS model using the experimentally measured slope. The calculated Stern layer thickness increases from Li^+ to Rb^+ and then decreases for Cs^+, in agreement with crystal radii data, but in disagreement with mobility measurements.[25] For all cations except Cs^+, the calculated Stern layer thickness is slightly greater than the cation-H_2O bond distance indicating that the Stern thickness is approximately equal to the radius of the first hydration shell for each of the respective cations. However, the calculated Stern layer thickness of Cs^+ is actually less than the measured Cs^+-H_2O distance, suggesting that Cs^+ is partially desolvated and specifically adsorbed on the Au surface under applied potential. Specific adsorption of Cs^+ has also been reported previously on Hg and Pt.[26–28] Specific adsorption also alters the polarization of the Cs^+ cation resulting in a change to the Onsager contribution to the total electric field. The result of specific adsorption, which causes Cs^+ to deviate from the uniform trend observed for the other cations in both the Stern and Onsager reaction fields, can be seen in Figures 2b and c, respectively.

To understand the correlation between Stern layer electric field, Stern layer thickness, Onsager reaction field, and CO_2R kinetics, we further investigated the role of cations on the selectivity and activity of CO_2R, as shown in Figure 3. We find excellent correlation between the Onsager reaction field and the selectivity and activity. Figure 3a and b shows linear sweep voltammetry (LSV) measurements and controlled potential electrolysis (CPE) measurements, respectively, with electrolytes containing CO_2 saturated Li^+, Na^+, K^+, Rb^+, and Cs^+ bicarbonates. The current density (Figure 3a) increases from Li^+,
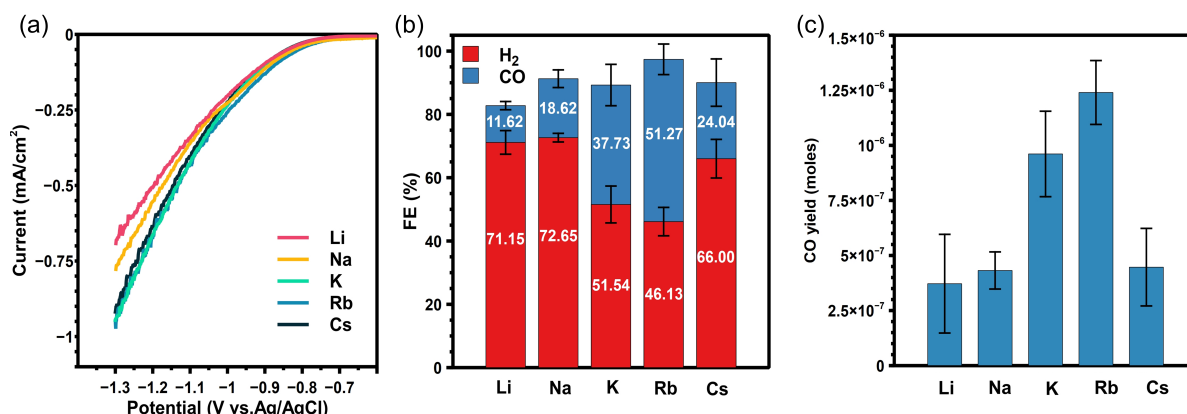
Figure 3. Kinetics measurement for each cation: a) Current density obtained by LSV measurement; b) Faradaic efficiency to CO and H_2 and c) CO yield obtained after 20 minutes at -1.2 V vs Ag/AgCl.

Na^+, to K^+, but remains almost unchanged for K^+, Rb^+ and Cs^+. However, the trend in CO Faradaic efficiency (FE) shows a volcano profile with Rb^+ at the maximum (Figure 3b). Surprisingly, this trend in catalytic performance is closely correlated with the Onsager reaction field and anti-correlated with the Stern layer electric field. There is no clear correlation between the measured reaction kinetics and the total electric field, and this observation is only possible after deconvolution of the Stern and Onsager fields. Although the significant increase of CO FE from Li^+ to Rb^+ has been observed before, the observed decrease in the presence of Cs^+ diverges from previous results, which reported Cs^+ to have similar CO FE to K^+ and Rb^+.[1,3] Figure 3c shows the CO production yield as a function of cation, which reflects the combined effect of current density and CO_2R selectivity. This plot highlights the significance of the cation effect, which results in a 4-fold increase in overall CO yield from Li^+ to Rb^+. However, Cs^+ represents an anomaly. Below we consider the reason for this anomaly and show that this is related to the change in interfacial solvation structure induced by specific adsorption of the Cs^+ cation as probed by the VSFG spectrum of interfacial water.
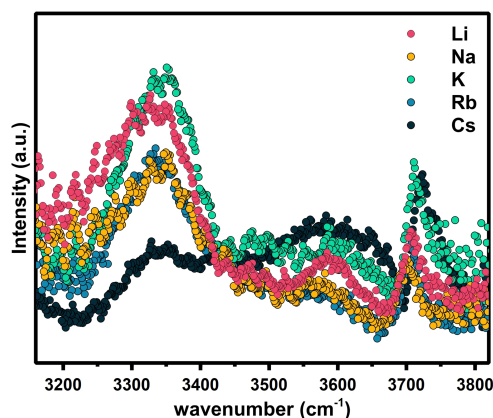

Figure 4. Water spectra obtained by vibrational sum frequecy generation for different alkali cations at -1.0 V vs. Ag/AgCl.

VSFG spectra of interfacial water were measured in-situ during CO_2R at -1.0 V vs. Ag/AgCl under CO_2R conditions (Figure 4). To our knowledge, these represent the first VSFG water spectra reported under electrocatalytic reaction conditions relevant for CO_2R. For comparison, the control experiment done with D_2O is provided in the supporting information section 4 confirming that none of these resonant features are observed in the absence of the H_2O in the aqueous electrolyte. Three peaks are apparent at around 3350 cm^{-1}, 3600 cm^{-1}, and 3700 cm^{-1}. The peak around 3200 cm^{-1} from "tetradedral" or ice-like water observed at the air/water interface[29–37] and dielectric/water interface[38–48] is missing in the spectra shown in Figure 4. This indicates a relatively disordered water structure at the gold electrode surface[49]. The peak at 3700 cm^{-1} is the dangling, or free OH; however, the assignment for the other peaks is the subject of ongoing debate.[29,30,34–36,50] It is generally considered that H-bonding lowers the vibrational frequencies of water, so the water feature at 3350 cm^{-1} can be assigned

either to liquid-like[31] water or to a H-bonding network with lower coordination compared to "tetradedral" water around 3200 cm^{-1},[33,38,43] while the peak at 3600 cm^{-1} can be attributed to more weakly H-bonded or singly H-bonded water.[30]

It is not the goal of the present report to provide a rigorous interpretation of these water spectra, which is the subject of ongoing work. Rather, we only comment on several marked correlations between these spectra, the Stern and Onsager contributions to total electric field, and the CO_2R reaction kinetics. First, we note that for cations Li^+, Na^+, K^+, and Rb^+, a similar overall spectrum is observed with intensity primarily at 3350 cm^{-1} and lesser intensity at 3600 cm^{-1}. Signal is also observed in the free OH region at 3700 cm^{-1}. In contrast, the water spectrum in the presence of Cs^+ is distinct from the other four cations, consistent with the effects of specific adsorption. In this case, we observe slightly higher intensity at 3600 cm^{-1} and significantly diminished intensity at 3350 cm^{-1}. One possible explanation for these changes is that specific adsorption of Cs^+ displaces interfacial water and disrupts H-bonding at the Au/electrolyte interface, resulting in decreased intensity of H-bonded water at 3350 cm^{-1}, although additional analysis will be required to confirm this interpretation. We note that $\chi^{(3)}$ will contribute to the measured water spectra due to the strong DC field present at these potentials.[51–54] However, the spectral changes measured here for Cs^+ cannot be explained solely by $\chi^{(3)}$ contributions. Because the total electric field is greatest in the presence of Cs^+ (see Figure 2a), this system should show the highest $\chi^{(3)}$ contribution from bulk water. In contrast, Cs^+ shows a significantly diminished intensity, suggesting instead a cation-induced change in the interfacial solvation structure. To summarize, we find that for cations Li^+ to Rb^+ displaying similar interfacial water structure, CO_2R kinetics closely follow the Onsager reaction field. However, for Cs^+ CO_2R rate is greatly diminished even though the Onsager reaction field is similar to that of Rb^+, and this anomaly is correlated with the effect of Cs^+ on the interfacial solvation structure.

Discussion

In light of these findings, we now consider the mechanism for effects of specific alkali cations on CO_2R kinetics. Several theories exist to explain these results, which can be categorized into two primary mechanisms: 1) Dipolar stabilization of CO_2^- by the interfacial electric field field[4,5,55] and 2) Cation-dependent hydrolysis reactions that act to buffer interfacial pH.[1,2,56] It has been noted that because the pKa of cation hydrolysis is electric field dependent, these two mechanisms may not be mutually exclusive.[1,25,57] Assuming that CO_2 activation depends only on dipolar stabilization of the bent CO_2^- intermediate, it is not possible to reconcile present results showing a correlation between reaction kinetcs and the Onsager field. Because electric field is a vector quantity, dipolar stabilization should be insensitive to the specific origins of the total field (i.e. Stern versus Onsager reaction fields). However, as noted in the second mechanism CO_2R kinetics are predicted to depend on the pKa of cation hydrolysis.[1,2] This is consistent with the present observation that cation-dependent selectivity tracks closely with the measured Onsager reaction field where the Onsager field depends on the cation polarizability, and cation polarizability in turn mediates the pKa of hydrolysis.[1,2] Accordingly, current findings are consistent with theoretical results by Bell et al.,[1] although the reason for this correlation must extend beyond the buffering capacity of specific cations to account for the dependence between CO_2R kinetics and interfacial water structure. This correlation is highlighted here for Cs^+, which displays low reaction selectivity despite having a relatively high value for Onsager reaction field, consistent with disruption of H-bonding at the electrode surface.

One possible explanation to reconcile these results is to assume that the rate-determining step in CO_2 involves transfer of a proton from a water molecule coordinated with the alkali cation. Water molecules coordinated to cations are known to have protons that vary in their acidity based on the presence of an electric field, with larger cations having a lower pKa, such that the barrier to proton transfer will be cation dependent.[1,2] Assuming that this proton is not donated from a hydronium ion but rather transfer occurs directly from a water molecule in the cation hydration shell, proton transfer will be independent of pH as confirmed experimentally.[56–58] Additionally, this model is consistent with the the observations reported here that disruption of the interfacial solvation structure by Cs^+ significantly hinders CO_2R. This is because CO_2R proton transfer kinetics depend on the availability of proton donors within the interfacial H-bonding network, and the H-bonding network will be influenced by changes in specific versus non-specific cations-surface interactions.

Overall, these data confirm that the interfacial solvation structure as well as the associated Onsager reaction field cannot be neglected when considering the kinetics of CO_2R. These findings call for additional models capable of treating solvation-mediated Onsager reaction fields and interfacial solvation structure on equal footing with the electric field produced by the DL. These data clearly show that accurate understanding of CO_2R kinetics at metal electrodes requires explicit treatment of interfacial solvation not present in continuum models, since these solvation structures result in significant changes in CO_2R kinetics as demonstrated here via direct, in-situ observation of the active Au/electrolyte interface.

.

Supporting Information

The supporting material contains information on the

1. Potential dependent SFG spectra of CO

2. Potential of zero charge measurements

3. Stark tuning slope and Stern layer thickness

4. VSFG spectra in the water region for $NaHCO_3$ in D_2O

Methods

1. Polycrystalline Au electrode preparation Two types of polycrystalline Au were used in this experiment. The Au electrodes for SFG measurement were manufactured by depositing 35 nm Au onto round CaF_2 windows through electron beam evaporation(Denton DV-502A E-Gun Evaporator). Before the Au deposition, the CaF_2 windows were cleaned with basic Piranha ($H_2O:H_2O_2:NH_4OH$ 5:1:1. Caution: Pirhana solutions are caustic and should be handled with extreme care) at 80 °C for one hour. The other type of Au electrodes (referred as Cr/Au), which were used for electrochemical measurements and FE measurement, were produced with the same equipment. The difference was that a 20 nm chromium adhesion layer was deposited onto the glass substrates before another layer of 100 nm Au was deposited on the top. Before each experiment, the Cr/Au was cleaned with ethanol and distilled water.

2. Sum frequency generation measurement

The sum frequency generation system has been described previously, however, we provide a brief description here.[10] The SFG system uses a Ti:Sapphire regenerative amplifire (Spectra Physics-Solstice) which outputs ∼90 fs pulses at 800 nm with a repetition rate of 2 kHz and with an average power of 3.5 W. Seventy percent of the output is used to pump an OPA (Topas Prime) which directs signal and idler to a non-collinear DFG stage. The remaining thirty percent is spectrally narrowed to ∼10 cm^{-1} using an air-gap Etalon (TecOptics). The beams are incident on the sample at 56 degrees in a Kretschmann configuration. The IR beam is centered at ∼2100 cm^{-1} in the CO region and has an energy of 3 μJ. In the water region the IR beam is centered at 2900 cm^{-1} and has an energy of 4 μJ and a beam area of 0.032 mm^2. The spectrally narrowed, 800 nm visible beam has an energy about 22 μJ, and a beam area of 0.128 mm^2. When measuring the CO spectra, a potential step ranging from -0.1V to -1.3 V vs. Ag/AgCl was applied to the Au electrode, and each spectrum was collected by delaying the visible beam relative to the IR beam for 850 fs, with an integration time of 1 min. For the water spectra, we integrated for 2 mins at a time delay of 500 fs.

3. Electrochemical measurements

Electrochemical measurements were made using a BioLogic SP-150 potentiostat. The electrochemical cell consisted of a Cr/Au electrode (WE), a leakless Ag/AgCl electrode (eDAQ ET072-1, RE), and a Pt mesh (CE). The electrolytes were prepared by purging 0.05 M M_2CO_3 (M=Li, Na, K, Rb, Cs, >99.9%, Sigma-Aldrich) with CO_2 (Praxair,99.9%) for 10 mins. For linear sweep voltammetry measurement, the potential was swept from 0 V to -1.3 V vs. Ag/AgCl with a scan rate of 50 mV/s. EIS measurements were taken at potentials in the range from 0.2 V to -0.6 V over a frequency range from 200 kHz to 100 mHz. The double layer capacitance was determined by fitting the EIS data with an equivalent circuit as suggested by Xie et al.[59] using ZView.
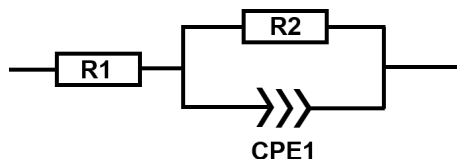

Figure 5. Equivalent circuit model used to fit EIS results

4. Gouy-Chapman-Stern model

The Gouy-Chapman-Stern model employed in this work is a combination of the classic Gouy-Chapman-Stern theory and the Stark tuning theory. The frequency shift ($\omega(\phi)$-ω_{PZC}) of a Stark reporter can be correlated with the potential drop ($\Delta\phi_S$) in the Stern layer by equation 2 below, where $\Delta\mu$ is the Stark tuning rate of CO (0.7 cm^{-1}/MV/cm), and d$_S$ is the Stern layer thickness. The potential drop in the Stern layer can be expressed by equation 3, where ϕ_o is the applied potential and ϕ_{OHP} is the potential at the outer Helmholtz plane (OHP). ϕ_o can be further correlated with ϕ_{OHP} by equation 4,[60] where ε is the dielectric

constant of water in the Stern layer (ε=6),[60] c is the concentration of cations, and z is the charge of the cation. The Stern layer thickness (d_S) and the potential at OHP (ϕ_{OHP}) can be solved from these three equations using the measured frequency of CO as an input.

$$\omega(\phi) = \omega_{PZC} + (\frac{\Delta\vec{\mu}}{d_S}) \cdot \Delta\phi_S \tag{2}$$

$$\Delta\phi_S = \phi_o - \phi_{OHP} \tag{3}$$

$$\phi_o - \phi_{OHP} = \frac{0.117 d_S}{\varepsilon\varepsilon_0} c^{1/2} sinh(19.4 z \phi_{OHP}) \tag{4}$$

5. Faradaic efficiency measurement

The measurement process for the Faradaic efficiency of CO and H_2 has been described elsewhere,[61] but we provide a summary here. An Agilent 7890B gas chromatograph was connected to the electrochemical H-cell through a headspace sampling system. The H-cell has two compartments, separated by a Nafion membrane. The Nafion membrane was activated in 10% H_2SO_4 at 80 C for 10 mins before each experiment. A Pt mesh was used as the counter electrode, and a Ag/AgCl electrode was used as the reference electrode. The electrolyte started with 0.05 M M_2CO_3 (M=Li, Na, K, Rb, Cs). At the beginning of the measurement, the electrolyte was purged with CO_2 for 10 mins to convert M_2CO_3 into $MHCO_3$, and the headspace of the H-cell was filled with CO_2. During CO_2R, a constant potential, i.e. -1.2V vs. Ag/AgCl, was applied to the Cr/Au working electrode for 20 mins by a BioLogical SP-50 potentialstat, before a gas sample from the headspace was injected into the GC. This process was repeated at least three times for each cation, and results were averaged the obtained FE of CO and H_2.

Acknowledgements

Author contributions statement

R.B. and S.W. conceived the experiments, Q.Z. conducted CPE, and LSV measurements. Q.Z. and S.W. conducted EIS and SFG Stark experiments, Q.Z., S.W. and G.D. analysed the results. Q.Z. and G.D. collected water spectra. All authors reviewed the manuscript.

Additional information

The authors declare no competing financial interests.

References

1. Singh, M. R., Kwon, Y., Lum, Y., Ager III, J. W. & Bell, A. T. Hydrolysis of electrolyte cations enhances the electrochemical reduction of CO_2 over Ag and Cu. *J. Am. Chem. Soc.* **138**, 13006–13012 (2016).

2. Ayemoba, O. & Cuesta, A. Spectroscopic evidence of size-dependent buffering of interfacial pH by cation hydrolysis during CO_2 electroreduction. *ACS Appl. Mater. Interfaces* **9**, 27377–27382 (2017).

3. Malkani, A. S., Anibal, J. & Xu, B. Cation effect on interfacial CO_2 concentration in the electrochemical CO_2 reduction reaction. *ACS Catal.* **10**, 14871–14876 (2020).

4. Gauthier, J. A. *et al.* Facile electron transfer to CO_2 during adsorption at the metal|solution interface. *J. Phys. Chem. C* **123**, 29278–29283 (2019).

5. Chen, L. D., Urushihara, M., Chan, K. & Nørskov, J. K. Electric field effects in electrochemical CO_2 reduction. *ACS Catal.* **6**, 7133–7139 (2016).

6. Ringe, S. *et al.* Double layer charging driven carbon dioxide adsorption limits the rate of electrochemical carbon dioxide reduction on gold. *Nat. Commun.* **11**, 1–11 (2020).

7. Bard, A. J. B. & Faulkner, L. R. *Electrochemical methods fundamentals and applications* (John Wiley & Sons, 2001).

8. Wallentine, S., Bandaranayake, S., Biswas, S. & Baker, L. R. Direct observation of carbon dioxide electroreduction on gold: Site blocking by the stern layer controls CO_2 adsorption kinetics. *J. Phys. Chem. Lett.* **11**, 8307–8313 (2020).

9. Sorenson, S. A., Patrow, J. G. & Dawlaty, J. M. Solvation reaction field at the interface measured by vibrational sum frequency generation spectroscopy. *J. Am. Chem. Soc.* **139**, 2369–2378 (2017).

10. Wallentine, S., Bandaranayake, S., Biswas, S. & Baker, L. R. Plasmon-resonant vibrational sum frequency generation of electrochemical interfaces: Direct observation of carbon dioxide electroreduction on gold. *J. Phys. Chem. A* **124**, 8057–8064 (2020).

11. Onsager, L. Electric moments of molecules in liquids. *J. Am. Chem. Soc.* **58**, 1486–1493 (1936).

12. Fried, S. D. & Boxer, S. G. Measuring electric fields and noncovalent interactions using the vibrational stark effect. *Acc. Chem. Res.* **48**, 998–1006 (2015).

13. Shi, H. *et al.* Monitoring local electric fields at electrode surfaces using surface enhanced raman scattering-based stark-shift spectroscopy during hydrogen evolution reactions. *ACS Appl. Mater. Interfaces* **10**, 33678–33683 (2018).

14. Yim, W.-L. *et al.* Universal phenomena of CO adsorption on gold surfaces with low-coordinated sites. *J. Phys. Chem. C* **111**, 445–451 (2007).

15. Yeh, I.-C. & Berkowitz, M. L. Dielectric constant of water at high electric fields: Molecular dynamics study. *J. Chem. Phys.* **110**, 7935–7942 (1999).

16. Levinson, N. M., Fried, S. D. & Boxer, S. G. Solvent-induced infrared frequency shifts in aromatic nitriles are quantitatively described by the vibrational stark effect. *J. Phys. Chem. B* **116**, 10470–10476 (2012).

17. van der Veken, B. J. *et al.* The nature of improper, blue-shifting hydrogen bonding verified experimentally. *J. Am. Chem. Soc.* **123**, 12290–12293 (2001).

18. Fried, S. D., Bagchi, S. & Boxer, S. G. Measuring electrostatic fields in both hydrogen-bonding and non-hydrogen-bonding environments using carbonyl vibrational probes. *J. Am. Chem. Soc.* **135**, 11181–11192 (2013).

19. Choi, J.-H. & Cho, M. Vibrational solvatochromism and electrochromism of infrared probe molecules containing $C \equiv O$, $C \equiv N$, C=O, or C-F vibrational chromophore. *J. Chem. Phys.* **134**, 154513 (2011).

20. Gunathunge, C. M., Ovalle, V. J. & Waegele, M. M. Probing promoting effects of alkali cations on the reduction of CO at the aqueous electrolyte/copper interface. *Phys. Chem. Chem. Phys.* **19**, 30166–30172 (2017).

21. Nightingale Jr, E. Phenomenological theory of ion solvation. effective radii of hydrated ions. *J. Phys. Chem.* **63**, 1381–1387 (1959).

22. Robinson, R. A. & Stokes, R. H. *Electrolyte solutions* (Courier Corporation, 2002).

23. Ringe, S. *et al.* Understanding cation effects in electrochemical CO_2 reduction. *Energy Environ. Sci.* **12**, 3001–3014 (2019).

24. Li, J., Li, X., Gunathunge, C. M. & Waegele, M. M. Hydrogen bonding steers the product selectivity of electrocatalytic CO reduction. *Proc. Natl. Acad. Sci. USA* **116**, 9220–9229 (2019).

25. Waegele, M. M., Gunathunge, C. M., Li, J. & Li, X. How cations affect the electric double layer and the rates and selectivity of electrocatalytic processes. *J. Chem. Phys.* **151**, 160902 (2019).

26. Frumkin, A. Influence of cation adsorption on the kinetics of electrode processes. *Trans. Faraday Soc.* **55**, 156–167 (1959).

27. Berkes, B. B., Inzelt, G., Schuhmann, W. & Bondarenko, A. S. Influence of Cs^+ and Na^+ on specific adsorption of *OH, *O, and *H at platinum in acidic sulfuric media. *J. Phys. Chem. C* **116**, 10995–11003 (2012).

28. Berkes, B., Székely, A. & Inzelt, G. Effect of Cs^+ ions on the electrochemical nanogravimetric response of platinum electrode in acid media. *Electrochem. Commun.* **12**, 1095–1098 (2010).

29. Raymond, E. A., Tarbuck, T. L., Brown, M. G. & Richmond, G. L. Hydrogen-bonding interactions at the vapor/water interface investigated by vibrational sum-frequency spectroscopy of $HOD/H_2O/D_2O$ mixtures and molecular dynamics simulations. *J. Phys. Chem. B* **107**, 546–556 (2003).

30. Gan, W., Wu, D., Zhang, Z., Feng, R. & Wang, H. Polarization and experimental configuration analyses of sum frequency generation vibrational spectra, structure, and orientational motion of the air/water interface. *J. Chem. Phys.* **124**, 114705 (2006).

31. Du, Q., Superfine, R., Freysz, E. & Shen, Y. Vibrational spectroscopy of water at the vapor/water interface. *Phys. Rev. Lett.* **70**, 2313 (1993).

32. Schnitzer, C., Baldelli, S. & Shultz, M. J. Sum frequency generation of water on NaCl, NaNO$_3$, KHSO$_4$, HCl, HNO$_3$, and H$_2$SO$_4$ aqueous solutions. *J. Phys. Chem. B* **104**, 585–590 (2000).

33. Liu, D., Ma, G., Levering, L. M. & Allen, H. C. Vibrational spectroscopy of aqueous sodium halide solutions and air-liquid interfaces: Observation of increased interfacial depth. *J. Phys. Chem. B* **108**, 2252–2260 (2004).

34. Sovago, M. *et al.* Vibrational response of hydrogen-bonded interfacial water is dominated by intramolecular coupling. *Phys. Rev. Lett.* **100**, 173901 (2008).

35. Feng, R., Guo, Y., Lu, R., Velarde, L. & Wang, H. Consistency in the sum frequency generation intensity and phase vibrational spectra of the air/neat water interface. *J. Phys. Chem. A* **115**, 6015–6027 (2011).

36. Nihonyanagi, S., Yamaguchi, S. & Tahara, T. Water hydrogen bond structure near highly charged interfaces is not like ice. *J. Am. Chem. Soc.* **132**, 6867–6869 (2010).

37. Strazdaite, S., Versluis, J. & Bakker, H. J. Water orientation at hydrophobic interfaces. *J. Chem. Phys.* **143**, 084708 (2015).

38. Kim, J. & Cremer, P. S. IR-visible SFG investigations of interfacial water structure upon polyelectrolyte adsorption at the solid/liquid interface. *J. Am. Chem. Soc.* **122**, 12371–12372 (2000).

39. Nihonyanagi, S., Ye, S. & Uosaki, K. Sum frequency generation study on the molecular structures at the interfaces between quartz modified with amino-terminated self-assembled monolayer and electrolyte solutions of various pH and ionic strengths. *Electrochim.Acta* **46**, 3057–3061 (2001).

40. Ostroverkhov, V., Waychunas, G. A. & Shen, Y. Vibrational spectra of water at water/α-quartz (0001) interface. *Chem. Phys. Lett.* **386**, 144–148 (2004).

41. Tian, C. & Shen, Y. Structure and charging of hydrophobic material/water interfaces studied by phase-sensitive sum-frequency vibrational spectroscopy. *Proc. Natl. Acad. Sci.* **106**, 15148–15153 (2009).

42. Becraft, K. A., Moore, F. G. & Richmond, G. L. Charge reversal behavior at the CaF$_2$/H$_2$O/SDS interface as studied by vibrational sum frequency spectroscopy. *J. Phys. Chem. B* **107**, 3675–3678 (2003).

43. Jena, K. C. & Hore, D. K. Variation of ionic strength reveals the interfacial water structure at a charged mineral surface. *J. Phys. Chem. C* **113**, 15364–15372 (2009).

44. Yang, Z., Li, Q., Gray, M. R. & Chou, K. C. Structures of water molecules at solvent/silica interfaces. *Langmuir* **26**, 16397–16400 (2010).

45. Backus, E. H., Schaefer, J. & Bonn, M. Probing the mineral–water interface with nonlinear optical spectroscopy. *Angew. Chem Int. Ed.* (2020).

46. Lis, D., Backus, E. H., Hunger, J., Parekh, S. H. & Bonn, M. Liquid flow along a solid surface reversibly alters interfacial chemistry. *Science* **344**, 1138–1142 (2014).

47. Tyrode, E. & Liljeblad, J. F. Water structure next to ordered and disordered hydrophobic silane monolayers: a vibrational sum frequency spectroscopy study. *J. Phys. Chem. C* **117**, 1780–1790 (2013).

48. DeWalt-Kerian, E. L. *et al.* pH-dependent inversion of Hofmeister trends in the water structure of the electrical double layer. *J. Phys. Chem. Lett.* **8**, 2855–2861 (2017).

49. Nihonyanagi, S. *et al.* Potential-dependent structure of the interfacial water on the gold electrode. *Surf. Sci.* **573**, 11–16 (2004).

50. Li, C.-Y. *et al.* In situ probing electrified interfacial water structures at atomically flat surfaces. *Nat. Mater.* **18**, 697–701 (2019).

51. Reddy, S. K. *et al.* Bulk contributions modulate the sum-frequency generation spectra of water on model sea-spray aerosols. *Chem* **4**, 1629–1644 (2018).

52. Ohno, P. E., Wang, H.-f. & Geiger, F. M. Second-order spectral lineshapes from charged interfaces. *Nat. Commun.* **8**, 1–9 (2017).

53. Jena, K. C., Covert, P. A. & Hore, D. K. The effect of salt on the water structure at a charged solid surface: Differentiating second-and third-order nonlinear contributions. *J. Phys. Chem. Lett.* **2**, 1056–1061 (2011).

54. Wen, Y.-C. *et al.* Unveiling microscopic structures of charged water interfaces by surface-specific vibrational spectroscopy. *Phys. Rev. Lett.* **116**, 016101 (2016).

55. Vijay, S. *et al.* Dipole-field interactions determine the CO$_2$ reduction activity of 2D Fe-N-C single-atom catalysts. *ACS Catal.* **10**, 7826–7835 (2020).

56. Zhang, F. & Co, A. C. Direct evidence of local pH change and the role of alkali cation during CO_2 electroreduction in aqueous media. *Angew. Chem. Int. Ed.* **59**, 1674–1681 (2020).

57. Chan, K. A few basic concepts in electrochemical carbon dioxide reduction. *Nat. Commun.* **11**, 1–4 (2020).

58. Varela, A. S. *et al.* pH effects on the selectivity of the electrocatalytic CO_2 reduction on graphene-embedded Fe-N-C motifs: Bridging concepts between molecular homogeneous and solid-state heterogeneous catalysis. *ACS Energy Lett.* **3**, 812–817 (2018).

59. Xie, X., Li, E. L. & Tang, Z. K. EQCM and EIS study of the effect of potential of zero charge on Escherichia coli biofilm development. *Int. J. Electrochem. Sci.* **5**, 1018–1025 (2010).

60. Elimelech, M. *et al.* Chapter 2-electrical properties of interfaces. *Part. Deposition & Aggreg.* 9–32 (1995).

61. Shang, H. *et al.* Effect of surface ligands on gold nanocatalysts for CO_2 reduction. *Chem. Sci.* **11**, 12298–12306 (2020).